

Combined Lidar-Radar Remote Sensing: Initial Results from CRYSTAL-FACE

M.J. McGill, L. Li, W.D. Hart, G.M. Heymsfield, D.L. Hlavka,

P.E. Racette, L. Tian, M.A. Vaughan, and D.M. Winker

Dr. Matthew J. McGill
NASA Goddard Space Flight Center, Code 912
Greenbelt, MD 20771
phone: 301-614-6281
fax: 301-614-5492
email: matthew.j.mcgill@nasa.gov

Dr. Lihua Li
University of Maryland Baltimore County GEST
NASA Goddard Space Flight Center, Code 912
Greenbelt, MD 20771
phone: 301-614-6356
fax: 301-614-5492
email: lihua@agnes.gsfc.nasa.gov

Mr. William D. Hart
Science Systems and Applications, Inc.
NASA Goddard Space Flight Center, Code 912
Greenbelt, MD 20771
phone: 301-614-6272
fax: 301-614-5492
email: billhart@virl.gsfc.nasa.gov

Dr. Gerald M. Heymsfield
NASA Goddard Space Flight Center, Code 912
Greenbelt, MD 20771
phone: 301-614-6369
fax: 301-614-5492
email: gerald.heymsfield@nasa.gov

Mr. Dennis L. Hlavka
Science Systems and Applications, Inc.

NASA Goddard Space Flight Center, Code 912
Greenbelt, MD 20771
phone: 301-614-6278
fax: 301-614-5492
email: sgdlh@virl.gsfc.nasa.gov

Mr. Paul E. Racette
NASA Goddard Space Flight Center, Code 555
Greenbelt, MD 20771
phone: 301-286-4756
fax: 301-286-1750
email: paul.e.racette@nasa.gov

Dr. Lin Tian
University of Maryland Baltimore County GEST
NASA Goddard Space Flight Center, Code 912
Greenbelt, MD 20771
phone: 301-614-6318
fax: 301-614-5492
email: tian@agnes.gsfc.nasa.gov

Mr. Mark A. Vaughan
Science Applications International Corp.
NASA Langley Research Center, Code 435
Hampton, VA 23681
phone: 757-864-5331
fax: 757-864-7775
email: m.a.vaughan@larc.nasa.gov

Dr. David M. Winker
NASA Langley Research Center, Code 435
Hampton, VA 23681
phone: 757-864-6747
fax: 757-864-7775
email: david.m.winker@nasa.gov

Submitted to Journal of Geophysical Research

July 31, 2003

Revised December 20, 2003

ABSTRACT

In the near future NASA plans to fly satellites carrying a two-wavelength polarization lidar and a 94-GHz cloud profiling radar in formation to provide complete global profiling of cloud and aerosol properties. The CRYSTAL-FACE field campaign, conducted during July 2002, provided the first high-altitude collocated measurements from lidar and cloud profiling radar to simulate these spaceborne sensors. The lidar and radar provide complementary measurements with varying degrees of vertical measurement overlap within cloud layers. This paper presents initial results of the combined airborne lidar-radar measurements during CRYSTAL-FACE. A comparison of instrument sensitivity is presented, within the context of particular CRYSTAL-FACE observations. It was determined that optically thin cirrus clouds are frequently missed by the radar, but are easily profiled with the lidar. In contrast, optically thick clouds and convective cores quickly extinguish the lidar signal but are easily probed with the radar. Results are presented to quantify the portion of atmospheric features sensed independently by each instrument and the portion sensed simultaneously by the two instruments. To capture some element of varying atmospheric characteristics, two cases are analyzed, one with convective systems and one having synoptic cirrus and considerable clear air. The two cases show quite different results, primarily due to differences in cloud microphysics.

INTRODUCTION

A series of satellites, flying in formation and providing synergistic data products, comprise NASA's future "A-train" constellation. The A-train takes its name from the Aqua satellite [Parkinson, 2003], which leads the string of satellites. Following Aqua are, in order, the CloudSat [Stephens *et al*, 2002], CALIPSO [Winker *et al*, 2003], PARASOL carrying the

POLDER instrument [Deschamps *et al*, 1994], and Aura [Schoeberl *et al*, 2001] satellites. These satellites will fly in a 705-km sun-synchronous orbit with an equatorial crossing time of 1:30 pm. This satellite formation is designed to combine complementary data products to provide improved global remote sensing of the atmosphere.

The Cirrus Regional Study of Tropical Anvils and Cirrus Layers - Florida Area Cirrus Experiment (CRYSTAL-FACE) field campaign during July 2002 [Jensen *et al*, 2003] deployed a comprehensive suite of instruments on six aircraft and at two ground sites to study tropical cirrus cloud properties and formation processes. Instruments onboard one of the aircraft, the NASA ER-2, provided high-altitude downlooking measurements from instruments that can be considered proxies for A-train instruments. The new Cloud Radar System (CRS) [Li *et al*, 2003a; Racette *et al*, 2003] is a 94 GHz pulsed Doppler radar and provides measurements similar to those of the CloudSat cloud profiling radar ([although CloudSat will not have Doppler capability](#)). The Cloud Physics Lidar (CPL) [McGill *et al*, 2002; McGill *et al*, 2003] provides measurements similar to the polarization-sensitive lidar on CALIPSO, which operates at 532 nm and 1064 nm. Detailed instrument descriptions can be found in the references, but fundamental instrument parameters are provided in Table 1. [We note that both CPL and CRS have higher vertical and spatial resolution than the future spaceborne instruments, which is a desirable feature for purposes of simulating the spaceborne systems' performance.](#)

In this work we examine selected CPL and CRS measurements from CRYSTAL-FACE, as these are the first high-altitude, collocated measurements from lidar and cloud profiling radar and can be used to assess the utility of future data products from CALIPSO and CloudSat. The combination of the two instruments, with wavelengths that differ by about three orders of

magnitude, is necessary to obtain a complete profile of clouds and aerosols. The radar is insensitive to aerosols and to clouds composed of small particles, but is highly sensitive to clouds composed of large ice crystals and can easily penetrate dense convective cloud. In contrast, lidar is sensitive to aerosols and to even the thinnest cloud layers, but cannot penetrate optically thick clouds. Because of its use of optical wavelengths, lidar can penetrate only to an optical depth of ~3-4, depending on instrument parameters. Similarities and differences in using the two techniques to remotely sense clouds are illustrated using data acquired during CRYSTAL-FACE on July 23 and July 26, 2002. The data acquired on July 23 represent unique measurements of a developing cirrus anvil, while on July 26 primarily non-convective cirrus was observed.

Combined lidar-radar measurements are not new,[e.g., Mace *et al.*, 1998; Comstock *et al.*, 2002] but the unique perspective and satellite simulation made possible from the high-altitude aircraft is new. There has been prior work devoted to developing retrieval algorithms using collocated lidar and radar data. For example, Wang and Sassen (2002a, 2002b) developed an algorithm to combine extinction profiles derived from lidar measurements with measurements of effective reflectivity provided by millimeter-wave radar to retrieve profiles of ice water content and characteristic particle size from cirrus clouds. The effectiveness of Wang and Sassen algorithm and other similar techniques is limited to regions where both the radar and the lidar have some measurement overlap in a cloud. It is useful, therefore, to begin quantifying this measurement overlap (how much overlap and how frequently), and to be useful to CALIPSO-CloudSat data products that quantification should occur based on data that simulates the satellite instruments. In this work we provide a spatial analysis that serves as an initial effort to assist researchers in their attempts to synthesize a complete understanding of cirrus clouds from the disparate measurements to be made by CALIPSO and CloudSat.

While ground-based observations show the utility of combining the two measurements, the high-altitude perspective provides a better approximation of the future CALIPSO-CloudSat data product. The primary benefit of using data from sensors on the ER-2 aircraft is that the instruments are above ~94% of the Earth's atmosphere and thus do not suffer the atmospheric attenuation inherent to ground-based sensors. The high-altitude measurements also provide invaluable data that is being used to develop and test the CALIPSO-CloudSat algorithms.

We emphasize that this work provides only an introduction to the combined measurements. Several research groups are currently using the CPL and CRS data to develop and test detailed retrieval algorithms for both CALIPSO-CloudSat operational processing and CRYSTAL-FACE science objectives. Results of these efforts are forthcoming. For now, however, there is a significant benefit to be gained from examining profiles made using the combined lidar and radar data, particularly as it relates to study of cirrus anvil development and evolution. Further, quantitatively relating the lidar and radar measurements in regions of measurement overlap (e.g., areas where the instruments simultaneously detect signal) is an important part of understanding how the instruments complement each other and has particular relevance to the future satellite missions.

COMBINED LIDAR-RADAR OBSERVATIONS

The CPL provides measurements with 30 m vertical by 1 s temporal resolution. At an average ER-2 ground speed of $\sim 200 \text{ ms}^{-1}$ the corresponding horizontal resolution is approximately 200 m. The CRS measurements are 37.5 m vertical by 0.5 s temporal resolution. Thus, the first step in

combining the CPL and CRS data is to match the spatial and temporal resolutions of the two data sets. For ease of computation, we chose to interpolate the CPL measurements to 37.5 m vertical resolution and to average the CRS measurements to 1 s temporal resolution.

The CPL measures at 355 nm, 532 nm and 1064 nm. However, only 532 nm data is used in this paper. The data at other wavelengths is similar and not presented here, and all of the lidar wavelengths are greatly separated from the millimeter radar wavelength. The lidar data inversion is detailed in McGill *et al.* (2003). Briefly, where possible the extinction profile and extinction-to-backscatter ratio were derived simultaneously using an iterative technique constrained by the measured two-way transmittance through cloud/aerosol layers. For those features not amenable to this approach, the extinction-to-backscatter ratio was prescribed and the extinction profile was derived following the method of Fernald.[Fernald, 1984]

Absolute calibration of radar systems is always a concern when attempting to draw comparisons with other instruments. Calibration of CRS was performed using a trihedral corner reflector. The calibration result was verified by intercomparison between CRS and the ground-based Cloud Profiling Radar System (CPRS) 95-GHz cloud radar of the University of Massachusetts-Amherst.[Sekelsky and McIntosh, 1996] The collocated measurements of the same clouds demonstrated consistency between the two instruments to better than 1 dB.[Li *et al.*, 2003b] In addition, CRS calibration was also verified using the ocean surface return and the X-band ER-2 Doppler Radar (EDOP), which has been well calibrated using the TRMM precipitation radar and the ocean surface return.[Heymsfield *et al.*, 1996; Heymsfield *et al.*, 2000]

A fundamental difficulty in combining data from lidar and radar is the difference in measured quantities. Whereas the lidar measures backscattered photons, or equivalently, profiles of attenuated backscatter, the radar measurement is quantified in terms of equivalent reflectivity. Thus, one aspect of this work is to relate the radar reflectivity to lidar-derived quantities such as backscatter and optical depth. The relative detectability of clouds between CRS and CPL is highly dependent on particle size. Cloud particles are in the Rayleigh and Mie scattering regimes at the CRS wavelength (3 mm), while they fall in the geometric range for the CPL wavelengths. Reflectivity of the millimeter-wave radar in the Rayleigh regime is proportional to the sixth power of the particle size. In the Mie regime the radar reflectivity is a function of both wavelength and particle size and therefore Mie scattering functions are used to calculate radar reflectivity. In contrast, lidar backscatter is proportional to the second power of the particle size. As a simple example consider a case where the total particle mass is conserved and the CRS is operating in the Rayleigh regime, and assume that particle radius decreases by a factor of two and the number concentration increases by a factor of eight. There are now smaller particles, but more of them. In this case, the lidar signal increases by a factor of two, while the radar signal decreases by a factor of eight. A comprehensive introduction to lidar and radar is beyond the scope of this paper, but an excellent reference (coincidentally focused on CloudSat and CALIPSO measurement synergy) is Okamoto *et al.* (2003).

Difficulties also arise when combining data from two separate sensors. In this case, many of the usual problems are remedied by having both CPL and CRS onboard the same aircraft. However, concerns such as pointing and footprint sizes are always present. Radar beam footprints are usually large compared with lidar, and that is the case here as well. The CPL receiver field of view is 100 microradians, so the receiver footprint at 20 km range is 2 m. The CRS has an

elliptical beam and at a range of 20 km the footprint is approximately 200 x 280 m. Although no attempt was made to precisely co-align the CPL and CRS, the disparity in footprint size provides wide margin in the pointing requirement. Due to the difference in footprint size, however, the lidar essentially subsamples the area sampled by the radar, [which can be important if there is small-scale cloud variability](#).

Before beginning detailed descriptions of the data, it is necessary to define some terminology. Because the radar signal does not incur significant attenuation in ice clouds and can penetrate most atmospheric cloud features, the radar data can be partitioned into two basic categories: (1) that within layers (e.g., cloud) and (2) clear air. For this work, radar cloud boundaries were determined using a thresholding technique similar to that described in Uttal *et al.* (1993). The lidar signal, however, can become completely extinguished when attempting to probe a dense cloud, so the lidar data are best partitioned into three categories: (1) that within layers, which for the lidar can be cloud, elevated aerosol or planetary boundary layer, (2) clear air, and (3) totally attenuated regions (e.g., the area beneath clouds that fully extinguish the lidar signal). The lidar layer boundaries were determined using a thresholding technique similar to that of Winker and Vaughan (1994). Finally, the lidar-derived optical depth is that due to aerosol and cloud and does not include molecular extinction (i.e., is particulate rather than total optical depth).

Having established definitions of layers, a description of the observations can now proceed. The initial focus for this study is the July 23 case from CRYSTAL-FACE because the ER-2 flew 8 passes along the same coordinates. The flight track, shown in Figure 1, was chosen to follow a developing convective cell and was intentionally chosen in the along-wind direction. The result is a unique data set showing growth and decay of the cirrus anvil over the course of a nearly 4-

hour period. This particular data set provides a good basis for combining lidar and radar data due to the range of conditions observed, including thick convective clouds, thin cirrus, and multiple cloud layering.

Figure 2 provides an initial comparison of the measurements acquired by the two instruments. The second column in Figure 2 shows the CPL data from the eight flight tracks. The data are plotted such that the images have common latitude-longitude end points even if the data does not extend to the end point. By plotting the data in this manner, it is easy to see the evolution of the convective system on a fixed latitude-longitude grid. In addition, every other image is plotted in reverse of the normal time scale to facilitate viewing on the fixed grid. In the first image two neighboring convective cells are seen, with a cirrus anvil starting to form. In successive images the convective cells collapse and decay while the cirrus anvil spreads downstream and decays into a complex multi-layered structure.

The CRS data is shown in the third column of Figure 2. Note that the convective core (e.g., on the right-hand side of the upper two panels) is easily observed by the radar whereas the lidar could not penetrate far into the cloud. Conversely, the radar is insensitive to much of the thin cirrus, even layers that are geometrically thick, which the lidar clearly senses. This is particularly apparent in the bottom three panels of Figure 2 between 12 km and 13.5 km, where the radar fails to detect all but a small fraction of the uppermost cirrus layer. The fourth column of Figure 2 shows the combined profiles generated from both CRS and CPL data. In these images yellow shading indicates regions where only the radar observed layers, blue shading indicates regions where only the lidar observed layers, and green shading is where both instruments observed

layers. Figure 2 thus provides a qualitative but visual indication of the instrument sensitivities and overlap between the measurements.

LIDAR-RADAR OBSERVATIONS: QUANTITATIVE RESULTS

Providing absolute comparisons of the lidar and radar measurements is difficult. A significant complication in comparing measurements from simple backscatter lidar and radar is that neither instrument is capable of directly measuring particle size or shape. Thus, there are three degrees of freedom in the atmospheric particulates (particle size, particle shape, and concentration) that affect each instrument signal in different ways as mentioned in the introduction. In particular, lidar is sensitive to equivalent particle diameter squared while, in the Rayleigh regime, the radar is sensitive to equivalent particle diameter to the sixth power. And, although depolarization measurements (which are obtained by both CPL and CRS) might be used to aid in comparing the lidar and radar data, such measurements are not unambiguous, since particle size and orientation can vary independently.

The 8 flight tracks of July 23, as shown in Figure 2, consist of a total of over 5 million range bins at 37.5 m vertical resolution (8927 profiles with 560 bins per profile at a flight altitude of 21 km). The radar detected cloud in 21.9% of the bins and clear air in the remaining 78.1%. The lidar profiles show that 10.7% of the radar clear air bins are actually not clear air but contain cloud (or aerosol) that was below the radar detection threshold. The lidar detected a layer in 15.3% of the bins, clear air in 52.2%, and in 32.5% of the bins had no signal because of overlying opaque cloud. From examining the radar data, a lower bound can be determined for the actual cloud amount contained in regions where the lidar signal was totally attenuated. In

this case, we find the radar detected clouds in 38.0% of the bins for which the lidar signal was totally attenuated.

Another way to analyze the detection capability of each instrument is to examine only those bins classified as being within a layer. Using just the bins within layers, 27.6% were observed by only the lidar while 22.8% were detected by both lidar and radar and 49.6% were detected by only the radar. These statistics are summarized in Table 2. In this particular case, the complementary nature of the measurements is evident and there is a fair degree of overlap between the instruments.

To illustrate characteristics of the lidar-radar vertical overlap, two particular profiles were selected from the third image segment in Figure 2 (indicated by vertical red lines on the combined image). Figure 3(a) shows a profile from 20:38:20 UTC, for a case where an optically thin cirrus cloud is found. In this example, the lidar detects two separate cirrus layers and penetrates through both (ground return was observed beneath). The radar does not detect the top cirrus layer, but does detect the lower portion of the second layer. The lidar cumulative optical depth reaches 0.25 before the radar begins to detect signal. Figure 3(b) shows a profile from 20:50:48 UTC. In this example the lidar signal is quickly attenuated by the dense clouds. Although the lidar detects the cirrus top before the radar does, the lidar signal is fully extinguished at 13 km altitude. The lidar cumulative optical depth reaches 0.15 before the radar signature begins. Figure 3 illustrates the complementary nature of the lidar and radar measurements, with the radar penetrating where the lidar cannot and the lidar sensitivity permitting observation of thin cirrus invisible to the radar. We note, however, that in both cases the lidar and radar both sense the core of the cirrus anvil primarily because anvils are

characterized by large aggregate ice clusters (often 600 microns and larger) that produce signals well within the detectability limit of both instruments.[Heymsfield *et al.*, 2000]

Analysis of many such profiles permits development of a relationship between lidar optical depth and radar minimum reflectivity. Figure 4 shows relationship between the topmost layer boundary determined from the radar and lidar data. In general the lidar detects the topmost layer boundary (i.e., that closest to the aircraft) before the radar. Thus, there is often a region of cirrus, which can be geometrically thick, that is undetected by the radar. Radiative effects of cirrus above convective cloud may be small compared to forcing from the convective cloud. In general, however, optically thin cirrus are radiatively significant [McFarquhar *et al.* 2000; Winker and Trepte, 1998] and underscore the need for the combination of lidar and radar profiling to provide more knowledge of the atmospheric column than is possible with either instrument alone. Figure 5 shows the fraction of occurrences of the lidar cumulative particulate optical depth not seen by the radar. The distribution shown in Figure 5 represents the cumulative optical depth down to the first bin detected by the radar. Figure 6 is a scatterplot illustrating the relationship between reflectivity and cumulative particulate optical depth. Although there is a trend there is also a large amount of scatter, presumably owing to large variability in particle characteristics, particularly particle size and shape.

It is illuminating to plot the lidar data as a distribution of the backscatter coefficient, as shown in Figure 7. Because most of the layers observed in this example are cloud as opposed to elevated aerosol, the histogram skews to higher backscatter coefficients. Overplotted in gray is the subset of lidar backscatter coefficients in regions sensed by both the lidar and the radar. Clearly the radar is most effective in regions with backscatter coefficient greater than $\sim 10^{-5} \text{ m}^{-1} \text{ sr}^{-1}$. Figure 8

is the subset of lidar backscatter coefficients, but only in layers that the radar did not detect, plotted as the fraction of occurrences not detected by the radar. Figure 8 demonstrates that the radar is good at detecting layers with backscatter coefficient $>10^{-5} \text{ m}^{-1} \text{ sr}^{-1}$ and the lidar is good at detecting regions with lower backscatter coefficient. We note that the distribution of backscatter coefficients in Figure 8 turns upwards at high backscatter there are a number of low-level cumulus clouds that the radar does not detect ([see discussion below](#)).

The case from July 23 is dominated by cirrus anvils in a tropical tropopause region and therefore limits the conclusions that can be drawn about the fractional overlap of the lidar and radar measurements for other cloud situations. To examine a contrasting case, data from July 26 were analyzed in the same manner as July 23. The July 26 flight was a survey flight south to 14 degrees North latitude. A composite lidar-radar image, similar to the right-hand column of Figure 2, is shown in Figure 9. The lidar detects a thick, extensive non-convective cirrus layer as well as elevated Saharan dust above the marine boundary layer. Note the lack of CRS detection, even over the geometrically thick cirrus at the southern end of the flight track. In regions with no detection by CRS, CPL estimates of cirrus optical depth are in the range 0.35-0.45 (+/- 0.14) for this cirrus cloud. Figure 9 shows only that portion of the July 26th data for which significant amounts of cloud or aerosol were detected, whereas the numbers given in Table 2 refer to statistics gathered over the entire flight. [The characteristics of ice particles in synoptic-scale cirrus are considerably different from those of cirrus associated with convective systems. The synoptic-scale cirrus typically have small, pristine ice crystals, often less than 100 microns in size.\[Heymsfield *et al.*, 1996\] The complex index of refraction is lower for ice particles than for water droplets, resulting in radar reflectivity that is lower, by several dB, for similar sized](#)

particles.[Lhermitte, 1990] The lower index of refraction coupled with the small size of pristine ice particles results in reflectivity that falls below the CRS detectability limit.

The July 26 data show a definite difference in characteristics compared to the July 23 data. Figure 10 shows the relation between reflectivity and lidar-derived cumulative particulate optical depth (cf. Figure 5). The difference is also reflected in the statistics given in Table 2, where the number of data bins within layers detected by the lidar only is more than double that of the July 23 case. A further illustration of the difference between the two cases is shown in Figure 11, which shows the distribution of CRS reflectivity for July 23 and July 26. In the July 23 case, as seen in Figure 2, there is cirrus but also considerable convective cloud. The July 26 case (recall Figure 9) is primarily cirrus with a small amount of convective cloud. For comparison, histograms of the lidar backscatter and that undetected by the radar are shown in Figures 12 and 13 (cf. Figures 7 and 8, respectively). In Figure 13 it appears that the radar misses a significant fraction of areas having high backscatter coefficient, but this is a misleading conclusion because there are only a small number of occurrences with high backscatter coefficient (use Figure 12 for proper context). The occurrences at high backscatter are due to low-level cumulus cloud detected by the lidar but not by the radar. The radar will typically not detect such cumulus owing to small droplet sizes (typically less than 100 microns diameter) that fall below the radar sensitivity limit.[Pruppacher and Klett (1997), Lhermitte (1990)] The CRS sensitivity, from data, versus altitude is -23.5 dBZe, -22.7 dBZe, and -17.1 dBZe at 3.5 km, 2.5 km, and surface, respectively. Thus, the small water droplets fall just at or below the limit of CRS detectability.

CONCLUSIONS

The CRYSTAL-FACE field campaign provided the first high-altitude collocated measurements from lidar and cloud profiling radar. Initial results of the combined lidar-radar measurements were shown, illustrating the complementary nature of the two instruments. Statistics derived from the measurements demonstrate the sensitivity of each instrument and the region of detection overlap between the instruments. The radar reflectivity was related to lidar-derived parameters such as optical depth. It was determined that optically thin cirrus clouds are frequently missed by the radar, but are easily profiled with the lidar. In contrast, optically thick clouds and convective cores quickly extinguish the lidar signal but are easily probed with the radar.

Most of the CRYSTAL-FACE flights were focused on convective systems and cirrus anvils. There was, however, one long flight that did not target convective systems. To capture some element of varying atmospheric characteristics, two cases were analyzed, one with convective systems and cirrus anvils and one having synoptic cirrus and considerable clear air. The two cases show quite different results, primarily due to differences in cloud distributions but also presumably because the ice hydrometeors have different characteristics. It follows that the best instrument for providing a complete profile of atmospheric clouds and aerosols is not a lidar or a radar, but a combination of both sensors. Future work, and work by other researchers, will combine the fundamental lidar and radar measurements to provide profiles of microphysical properties, such as effective particle diameter and ice water content, that are of importance to climate models and 3-D simulations. The combination of CPL and CRS measurements from CRYSTAL-FACE gives a first glimpse of the combined data product from the future CALIPSO and CloudSat missions and provides a clear indicator of the measurement synergy that exists between these two remote sensing methods.

ACKNOWLEDGEMENTS

The Cloud Physics Lidar is sponsored by NASA's Radiation Sciences Program (Code YS) and by NASA's Earth Observing System (EOS) office. The Cloud Radar System is sponsored by NASA's Radiation Sciences Program (Code YS). Data presented was collected as part of the Cirrus Regional Study of Tropical Anvils and Cirrus Layers - Florida Area Cirrus Experiment (CRYSTAL-FACE) field campaign.

REFERENCES

Comstock, J.M., T.P. Ackerman, and G.G. Mace: "Ground-based lidar and radar remote sensing of tropical cirrus clouds at Nauru Island: Cloud statistics and radiative impacts," *Journal of Geophysical Research*, **107**, doi:10.1029/2002JD002203, 2002.

Deschamps, P.Y., F.M. Breon, M. Leroy, A. Podaire, A. Bricaud, J.C. Buriez, and G. Seze, "The POLDER mission: Instrument characteristics and scientific objectives," *IEEE Transactions on Geoscience and Remote Sensing*, **32**, 598-615, 1994.

[Fernald 1984.](#)

Heymsfield, A.J., and G.M. McFarquhar: "High albedos of cirrus in the tropical Pacific Warm Pool: Microphysical interpretations from CEPEX and from Kwajalein, Marshall Islands," *Journal of the Atmospheric Sciences*, **53**, 2424-2451, 1996.

Heymsfield, A.J., A. Bansemer, P.R. Field, S.L. Durden, J.L. Stith, J. E. Dye, W. Hall, and C.A. Grainger: “Observations and parameterizations of particle size distributions in deep tropical cirrus and stratiform precipitating clouds: Results from in situ observations in TRMM field campaigns,” *Journal of the Atmospheric Sciences*, **59**, 3457-3491, 2002.

Heymsfield, G.M., S.W. Bidwell, I.J. Caylor, A.S. Nicholson, W.C. Boncyk, L. Miller, D. Vandemark, P.E. Racette, and L.R. Dod: “The EDOP radar system on the high-altitude NASA ER-2 aircraft,” *Journal of Atmospheric and Oceanic Technology*, **13**, 795-809, 1996.

Heymsfield, G.M., B. Geerts and L. Tian: “TRMM precipitation radar reflectivity profiles as compared with high-resolution airborne and ground-based radar measurements,” *Journal of Applied Meteorology*, **39**, 280-2102, 2000.

Jensen, E.J., D.E. Anderson, H.B. Selkirk, D.O. Starr, and O.B. Toon, “Overview of the Cirrus Regional Study of Tropical Anvils and Cirrus Layers – Florida Area Cirrus Experiment (CRYSTAL-FACE),” *Bulletin of the American Meteorological Society*, 2003 (submitted).

Lhermitte, R.: “Attenuation and scattering of millimeter wavelength radiation by clouds and precipitation,” *Journal of Atmospheric and Oceanic Technology*, **7**, 464-479, 1990.

Li, L., G.M. Heymsfield, P.E. Racette, L. Tian, and E. Zenker, “The 94 Ghz Cloud Radar System on the NASA ER-2 Aircraft,” *Journal of Atmospheric and Oceanic Technology*, 2003a (submitted).

Li, L., G.M. Heymsfield, P.E. Racette, L. Tian, and E. Zenker: "An airborne 94-GHz cloud radar on a NASA ER-2," *Journal of Atmospheric and Oceanic Technology*, 2003b (submitted).

Mace, G.G., K. Sassen, S. Kinne, and T.P. Ackerman: "An examination of cirrus cloud characteristics using data from millimeter wave radar and lidar," *Geophysical Research Letters*, **25**, 1133, 1998.

McFarquhar, G.M., A.J. Heymsfield, J. Spinhirne, and W. Hart, "Thin and subvisual tropopause tropical cirrus: observations and radiative impacts," *Journal of the Atmospheric Sciences*, **57**, 1841-1853 (2000).

McGill, M.J., D.L. Hlavka, W.D. Hart, V.S. Scott, J.D. Spinhirne, and B. Schmid, "The Cloud Physics Lidar: instrument description and initial measurement results," *Applied Optics*, **41**, 3725-3734, 2002.

McGill, M.J., D.L. Hlavka, W.D. Hart, E.J. Welton, and J.R. Campbell, "Airborne lidar measurements of aerosol optical properties during SAFARI-2000," *Journal of Geophysical Research*, **108**, doi: 10.1029/2002JD002370, 2003.

Okamoto, H., S. Iwasaki, M. Yasui, H. Horie, H. Kuroiwa, and H. Kumagai, "An algorithm for retrieval of cloud microphysics using 95-GHz cloud radar and lidar," *Journal of Geophysical Research*, **108**, doi: 10.1029/2001/JD001225, 2003.

Parkinson, C.L., "Aqua: An Earth-observing satellite mission to examine water and other climate variables," *IEEE Transactions on Geoscience and Remote Sensing*, **41**, 173-183, 2003.

Pruppacher, H.R., J.D. Klett: "Microphysics of Clouds and Precipitation", Kluwer Academic Publishers, Boston, 954 pp. , 1997.

(section 2.1.3 of relevance).

Racette, P.E., G.M. Heymsfield, L. Li, L. Tian, and E. Zenker, "The Cloud Radar System," in *Proceedings of the 31st AMS conference on Radar Meteorology*, Seattle, WA, August 2003.

Sekelsky, S.M. and R.E. McIntosh: "Cloud observations with polarimetric 33 GHz and 95 GHz radar," *Meteorology and Atmospheric Physics*, **59**, 123-140, 1996.

Schoeberl, M.R., A.R. Douglass, E. Hilsenrath, J. Barnett, R. Beer, J. Waters, J. Gille, P. Levelt, P. DeCola, "The EOS Aura Mission," in *IGARSS 2001: Scanning the Present and Resolving the Future*, (New York: IEEE), 227-232, 2001.

Stephens, G.L., D.G. Vane, R.J. Boain, G.G. Mace, K. Sassen, Z. Wang, A.J. Illingworth, E.J. O'Connor, W.B. Rossow, S.L. Durden, S.D. Miller, R.T. Austin, A. Benedetti, C. Mitrescu, and the CloudSat Science Team, The CloudSat Mission and the A-Train: A New Dimension of Space-Based Observations of Clouds and Precipitation, *Bulletin of the American Meteorological Society*, **83**, 1771-1790, 2002.

Uttal, T., L.I. Church, B.E. Martner, and J.S. Gibson, "CLDSTATS: A Cloud Boundary Detection Algorithm for Vertically Pointing Radar Data," NOAA Technical Memorandum ERL WPL-233, Wave Propagation Laboratory, Boulder, CO, July 1993.

Wang, Z., and K. Sassen: "Cirrus cloud microphysical property retrieval using lidar and radar measurements: I. Algorithm description and comparison with in situ data," *Journal of Applied Meteorology*, **41**, 218-229, 2002a.

Wang, Z., and K. Sassen: "Cirrus cloud microphysical property retrieval using lidar and radar measurements: II. Midlatitude cirrus microphysical and radiative properties," *Journal of the Atmospheric Sciences*, **59**, 2291–2302, 2002b.

Winker, D.M. and M.A. Vaughan, "Vertical distribution of clouds over Hampton, Virginia, observed by lidar under the ECLIPS and FIRE ETO programs," *Atmospheric Research*, **34**, 117-133, 1994.

Winker, D.M. and C.R. Trepte: "Laminar cirrus observed near the tropical tropopause by LITE," *Geophysical Research Letters*, **25**, 3351-3354, 1998.

Winker, D.M., J. Pelon and M.P. McCormick: "The CALIPSO Mission: spaceborne lidar for observation of aerosols and clouds," in *Proceedings of SPIE*, Vol. 4893 (U. Singh, T. Itabe, Z. Liu eds.), 1-11, Hangzhou, China, 24-25 October 2002.

FIGURE CAPTIONS

Figure 1: ER-2 flight track for July 23, 2002. Red curve is the entire flight track; thick black lines are the segments shown in Figures 2 and 3.

Figure 2: First column shows ER-2 flight track for each image. Arrows indicate direction of travel. Second column shows profiles of CPL 532 nm attenuated backscatter coefficient. Each image is the same length and covers the same latitude-longitude interval. Note that data from westbound flight legs (images 2, 4, 6, 8) has been reversed to allow direct comparison with the eastbound flight legs. Plotted in this manner, it is easy to see evolution of the convective system and anvil in a fixed coordinate system. Third column shows profiles of CRS reflectivity. Fourth column is the combined lidar and radar image. Blue color shading indicates regions where only CPL detected layers; yellow color shading indicates regions where only CRS detected layers; green shading indicates regions where both CRS and CPL detected layers (i.e., the instrument overlap). The combined images show cloud/aerosol layers only (e.g., background atmosphere is removed from the lidar data).

[NOTE: intent is to have Figure 2 printed as a 2-page spread to allow easy viewing.]

Figure 3: (a) Profiles from 20:38:20 UTC and (b) profiles from 20:50:48 UTC, July 23, 2002. Solid black line is the CRS radar reflectivity. Light gray dashed line is the CPL lidar attenuated backscatter profile and gray dashed line is the lidar-derived cumulative particulate optical depth. Data is only shown within regions determined to be cloud layers. The profile from 20:38:20 illustrates the case of optically thin cirrus that the lidar fully detects. The profile at 20:50:48 shows the case of an optically thick cloud that the lidar cannot penetrate but the radar can profile.

Figure 4: Comparison of topmost layer height from July 23, 2002 showing the lidar frequently detects layer boundaries before the radar.

Figure 5: Occurrences of cumulative particulate optical depth derived from lidar measurements in regions of no radar detection, for July 23, 2002. Histogram shows all optical depths missed by the radar (e.g., optical depth down to the first bin detected radar, or entire profile if radar detected no signal).

Figure 6: Scatterplot of radar reflectivity versus lidar-derived cumulative particulate optical depth, for July 23, 2002. Gray line is best fit (χ^2) to the data. Although there is a trend to higher optical depth with increasing reflectivity, there is also a large degree of scatter.

Figure 7: Distribution of backscatter coefficients from all lidar measurements within layers (black histogram), from July 23, 2002. Overplotted in gray is the subset detected by the lidar in regions where there was also valid radar signature (i.e., the measurement overlap).

Figure 8: Distribution of backscatter coefficients from lidar in regions where the radar did not detect valid signal, for July 23, 2002. This is a distribution of backscatter missed by the radar, plotted as a fraction of occurrences. The distribution turns upwards at high backscatter because the lidar detects low-level cumulus cloud that the radar does not detect.

Figure 9: Composite image for July 26, 2002. Only the middle half of the flight is shown, as there was no radar signature in the early and later portions of the flight. The black region masks

a 180-degree turn at the southern end of the flight track. Regions shaded in blue indicate detection by lidar only, yellow indicated detection by radar only, and green indicates detection by both. Note that in contrast the July 23 case, there is less measurement overlap in this example. The bottom panel is an enlarged view of the lowest two km over a short 5 minute segment showing that the lidar detected low-level cumulus of small vertical and spatial extent. Such cumulus are not detected by the radar owing to small particle size.

Figure 10: Occurrences of cumulative particulate optical depth derived from lidar measurements in regions of no radar detection, for July 26, 2002. Histogram shows all optical depths missed by the radar (e.g., optical depth down to the first bin detected radar, or entire profile if radar detected no signal). Compare with Figure 5 from July 23.

Figure 11: (a) Distribution of CRS radar reflectivity for July 23, 2002. (b) Same, for July 26, 2002. In each case, the black histogram is all bins detected by the radar. Overplotted in gray is the subset of bins from regions where the lidar also detected valid data.

Figure 12: Distribution of backscatter coefficients from all lidar measurements within layers (black histogram), from July 26, 2002. Overplotted in gray is the subset detected by the lidar in regions where there was also valid radar signature (i.e., the instrument overlap). Compare with Figure 7 from July 23.

Figure 13: Distribution of backscatter coefficients from lidar in regions where the radar did not detect valid signal, for July 26, 2002. This is a distribution of backscatter missed by the radar, plotted as a fraction of occurrences. The distribution turns upwards at high backscatter because

on this day the lidar detected considerable low-level cumulus cloud that the radar does not detect.
Compare with Figure 8 from July 23.

Table 1: Primary instrument specifications for CRS and CPL.

CRS Parameters	
frequency	94.155 GHz
RF peak power	1.7 kW
pulse repetition frequency (PRF)	4 kHz/5kHz, dual PRF
minimum range resolution	37.5 m
temporal resolution	1/2 s raw data, 1 s processed data
antenna beamwidth (cross track x along track)	0.6 x 0.8 degrees
sensitivity (with 150 m range resolution and 1 s averaging)	-35 dBZe at 5 km range -29 dBZe at 10 km range -17 dBZe at 20 km range
<hr/>	<hr/>
CPL Parameters	
wavelengths and output energy	1064 nm, 50 μ J 532 nm, 25 μ J 355 nm, 50 μ J
pulse repetition rate	5 kHz
minimum range resolution	30 m
temporal resolution	1/10 s raw data, 1 s processed data
telescope diameter	20 cm

receiver field of view	100 microradians (full angle)
minimum detectable backscatter (532 nm)	cirrus (daytime): $1.2 \times 10^{-7} \text{ m}^{-1} \text{ sr}^{-1}$ cirrus (nighttime): $5.0 \times 10^{-8} \text{ m}^{-1} \text{ sr}^{-1}$ aerosol (daytime): $3.1 \times 10^{-7} \text{ m}^{-1} \text{ sr}^{-1}$ aerosol (nighttime): $6.8 \times 10^{-8} \text{ m}^{-1} \text{ sr}^{-1}$

Table 2: Statistics from July 23 and July 26 cases.

	July 23	July 26
total number of profiles used	8927	13760
total number of possible data elements (bins)	5,000,719	7,373,469
radar: % total bins with data in layers	21.9%	2.3%
radar: % total bins in clear air	78.1%	97.7%
lidar: % total bins with data in layers	14.8%	5.5%
lidar: % total bins in clear air	26.7%	91.0%
lidar: % total bins fully attenuated	58.6%	3.5%
_____	_____	_____
% bins detected by lidar only (within layers)	27.6%	67.4%
% bins detected by both lidar and radar (within layers)	22.8%	10.4%
% bins detected by radar only (within layers)	49.6%	22.2%

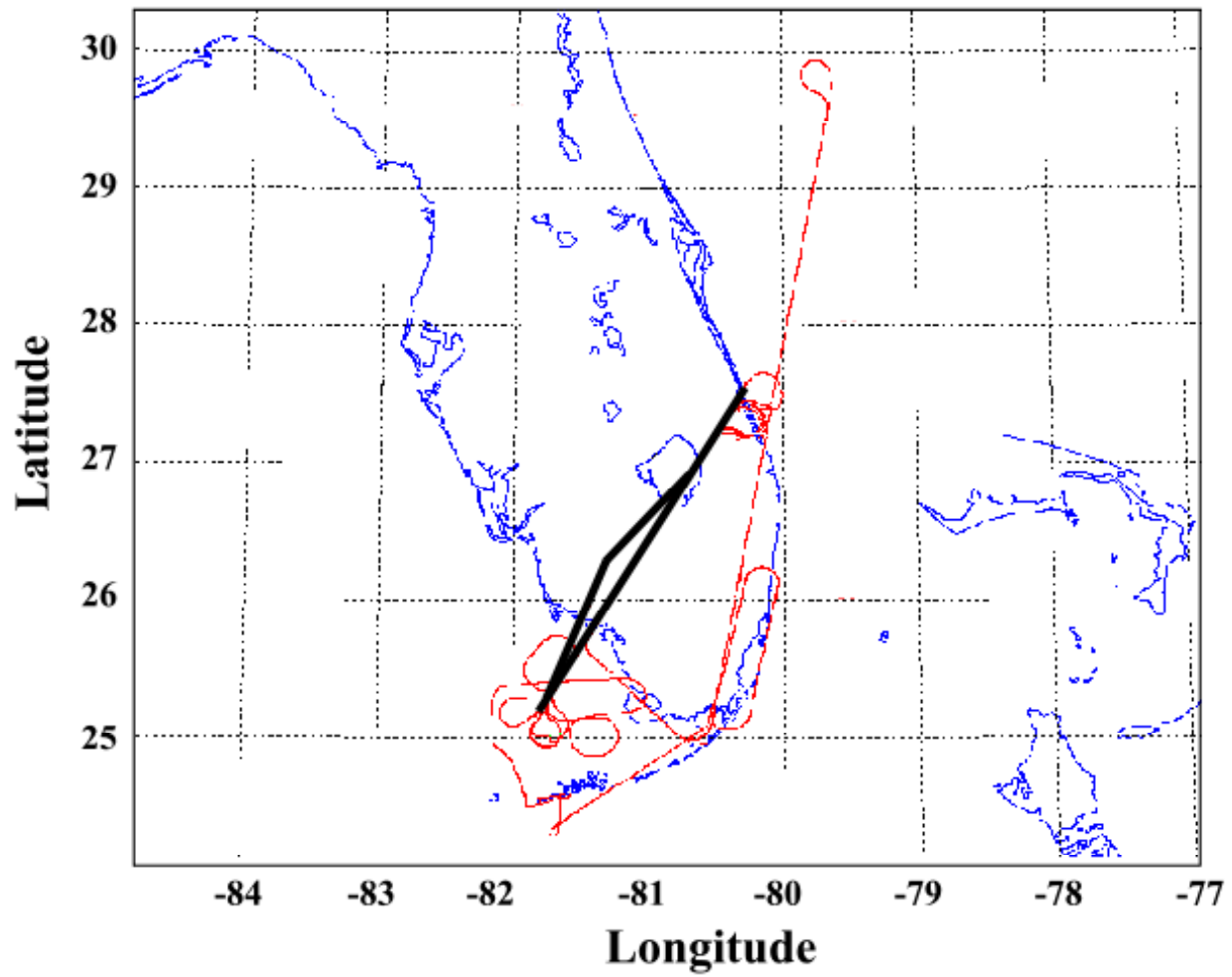


Figure 1: ER-2 flight track for July 23, 2002. Red curve is the entire flight track; thick black lines are the segments shown in Figures 2 and 3.

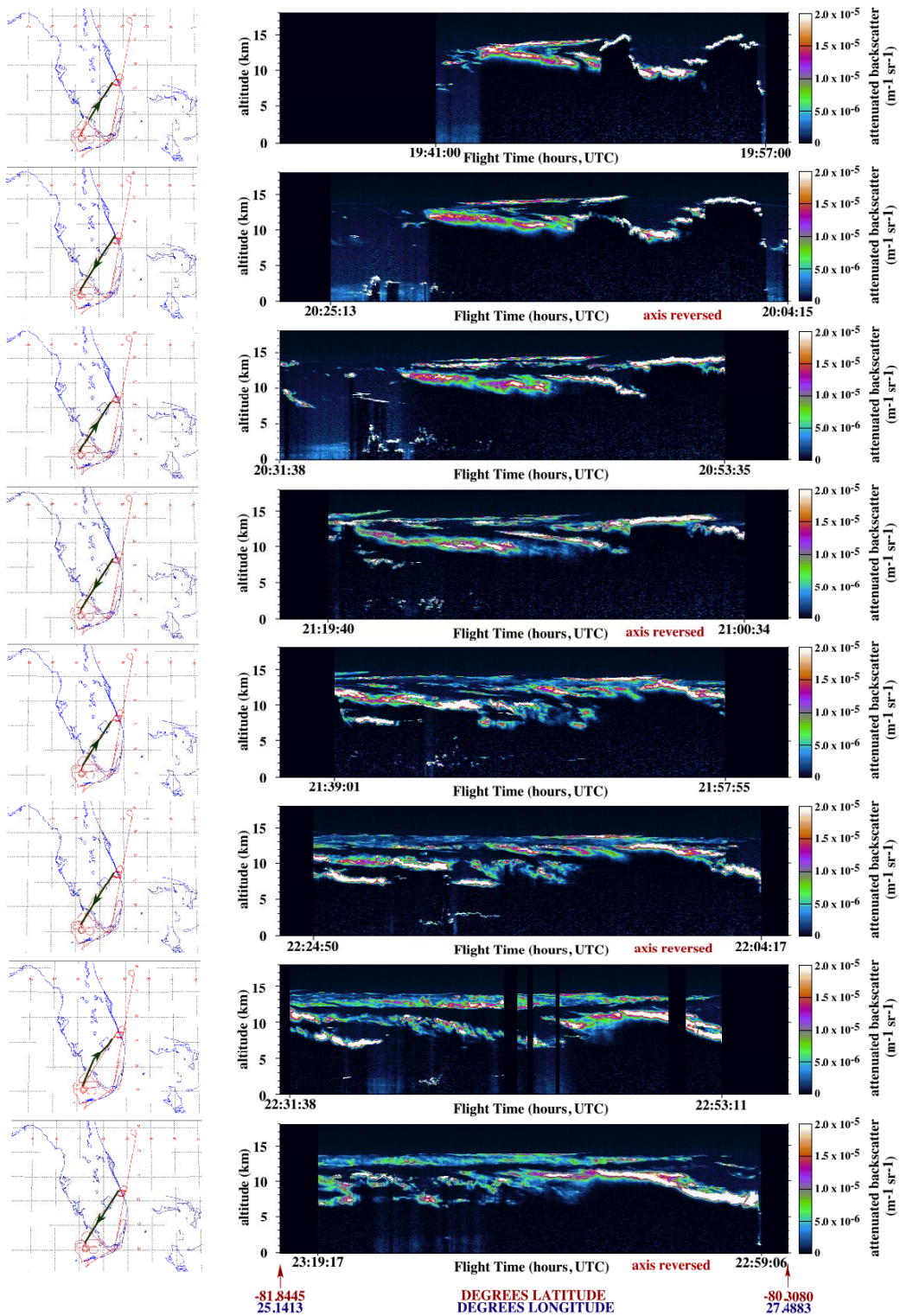


Figure 2: First column shows ER-2 flight track for each image. Arrows indicate direction of travel. Second column shows profiles of CPL 532 nm attenuated backscatter coefficient. Each image is the same length and covers the same latitude-longitude interval. Note that data from westbound flight legs (images 2, 4, 6, 8) has been reversed to allow direct comparison with the eastbound flight legs. Plotted in this manner, it is easy to see evolution of the convective system and anvil in a fixed coordinate system. (caption continued below)

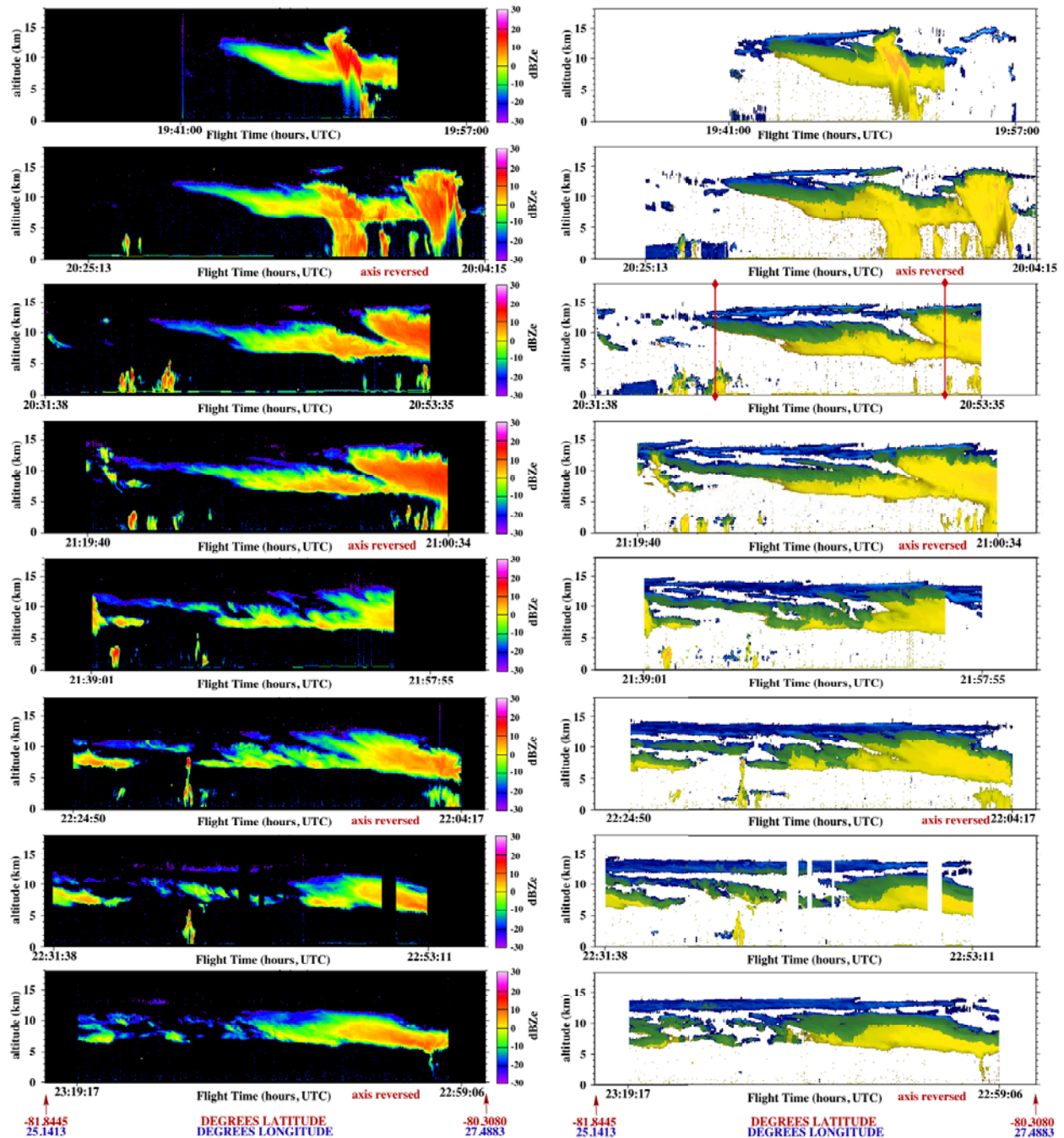


Figure 2 (con't): Third column shows profiles of CRS reflectivity. Fourth column is the combined lidar and radar image. Blue color shading indicates regions where only CPL detected layers; yellow color shading indicates regions where only CRS detected layers; green shading indicates regions where both CRS and CPL detected layers (i.e., the instrument overlap). The combined images show cloud/aerosol layers only (e.g., background atmosphere is removed from the lidar data).

[NOTE: intent is to have Fig. 2 printed as a 2-page spread.]

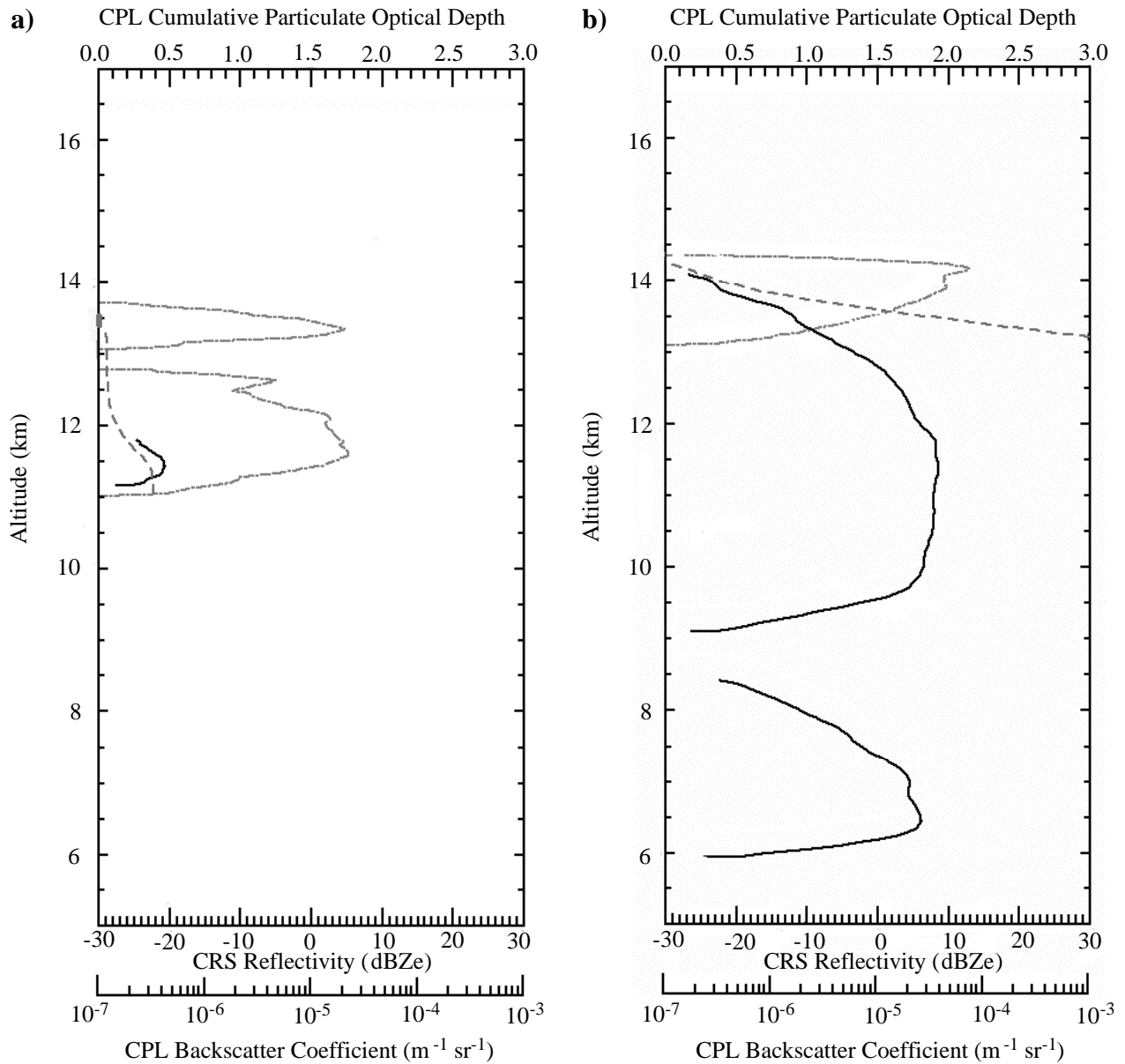


Figure 3: (a) Profiles from 20:38:20 UTC and (b) profiles from 20:50:48 UTC, July 23, 2002. Solid black line is the CRS radar reflectivity. Light gray dashed line is the CPL lidar attenuated backscatter profile and gray dashed line is the lidar-derived cumulative particulate optical depth. Data is only shown within regions determined to be cloud layers. The profile from 20:38:20 illustrates the case of optically thin cirrus that the lidar fully detects. The profile at 20:50:48 shows the case of an optically thick cloud that the lidar cannot penetrate but the radar can profile.

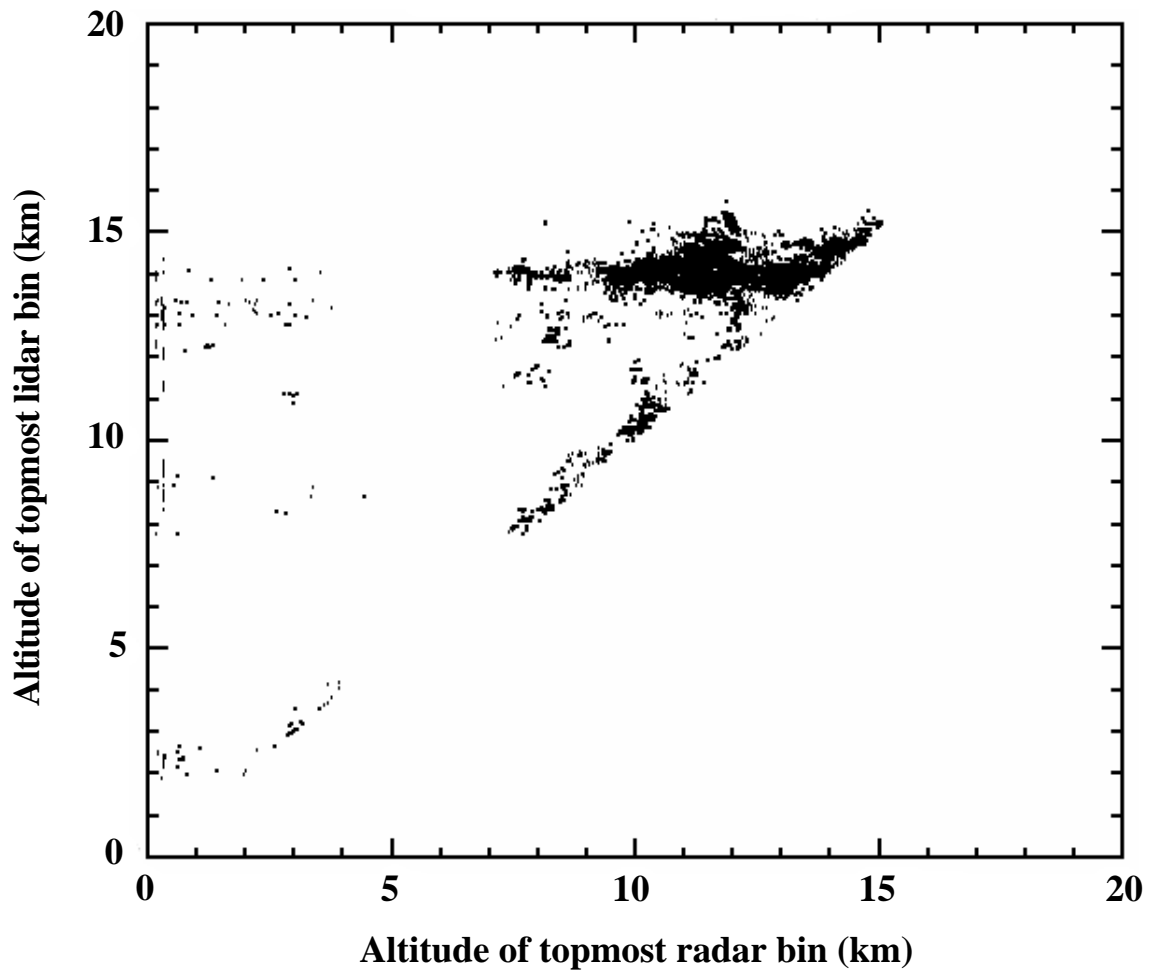


Figure 4: Comparison of topmost layer height from July 23, 2002 showing the lidar frequently detects layer boundaries before the radar.

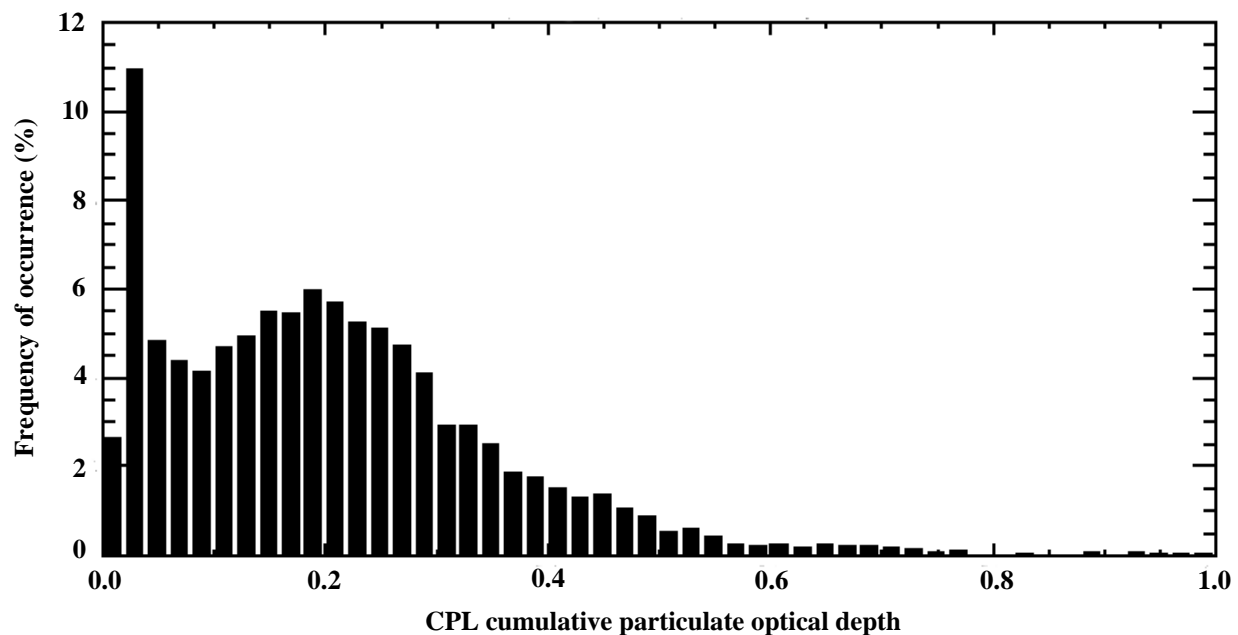


Figure 5: Occurrences of cumulative particulate optical depth derived from lidar measurements in regions of no radar detection, for July 23, 2002. Histogram shows all optical depths missed by the radar (e.g., optical depth down to the first bin detected by radar, or entire profile if radar detected no signal).

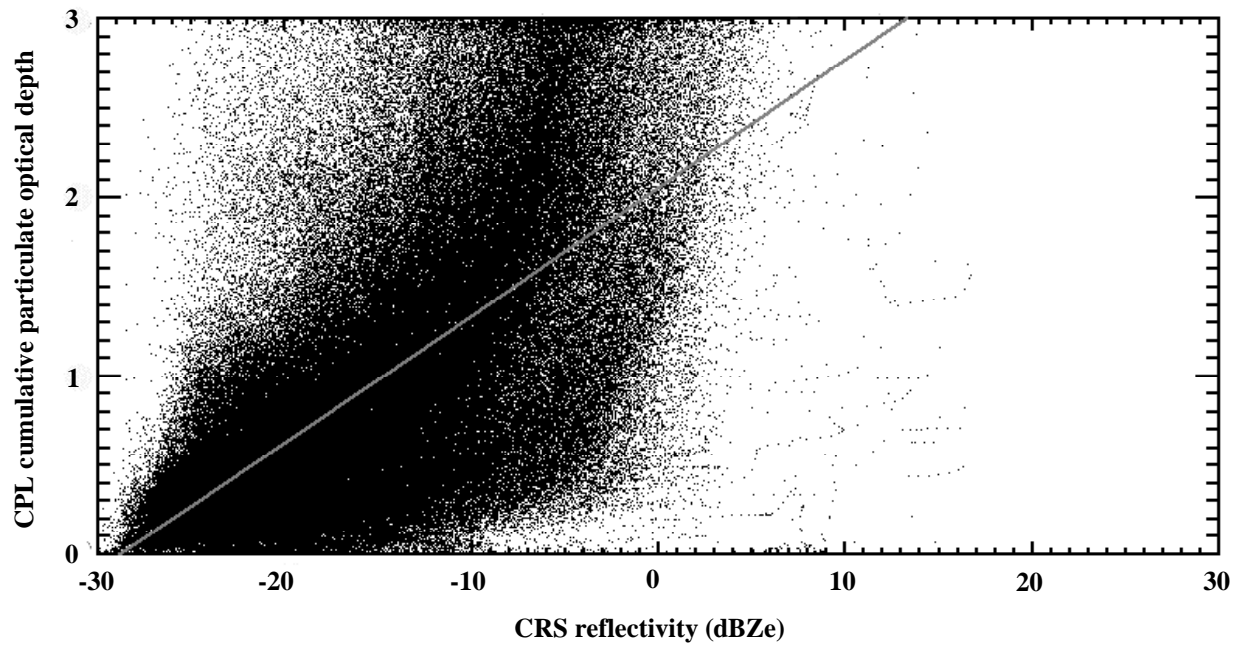


Figure 6: Scatterplot of radar reflectivity versus lidar-derived cumulative particulate optical depth, for July 23, 2002. Gray line is the best fit (χ^2) to the data. Although there is a trend to higher optical depth with increasing reflectivity, there is also a large degree of scatter.

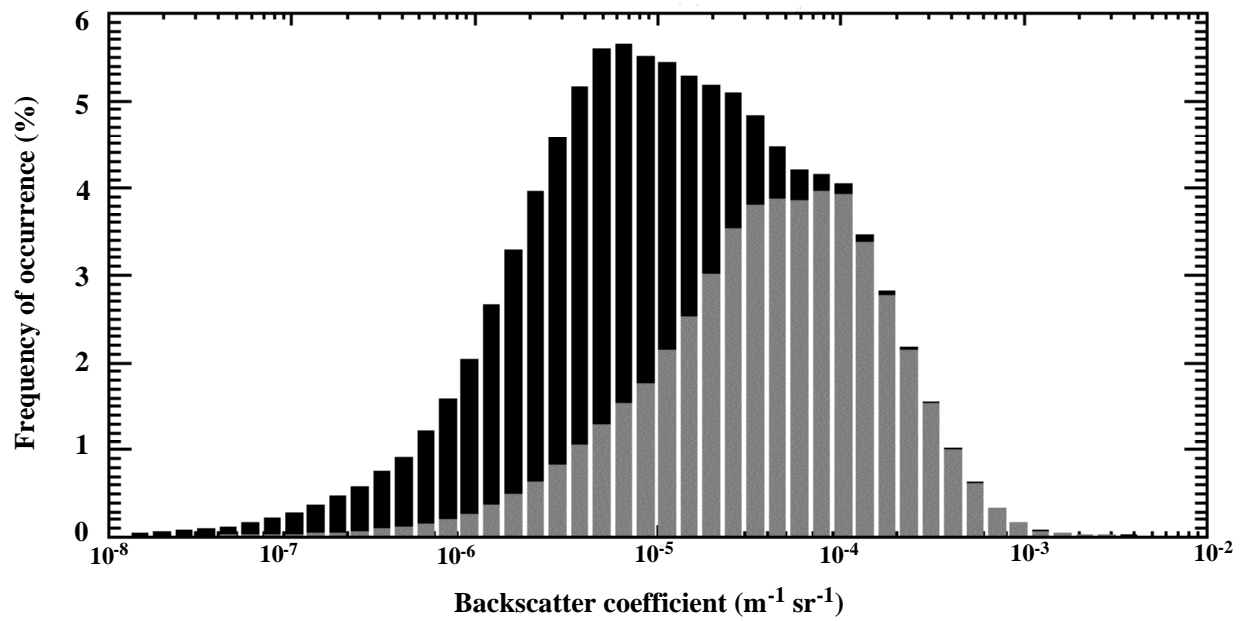


Figure 7: Distribution of backscatter coefficients from all lidar measurements within layers (black histogram), from July 23, 2002. Overplotted in gray is the subset detected by the lidar in regions where there was also valid radar signature (i.e., the measurement overlap).

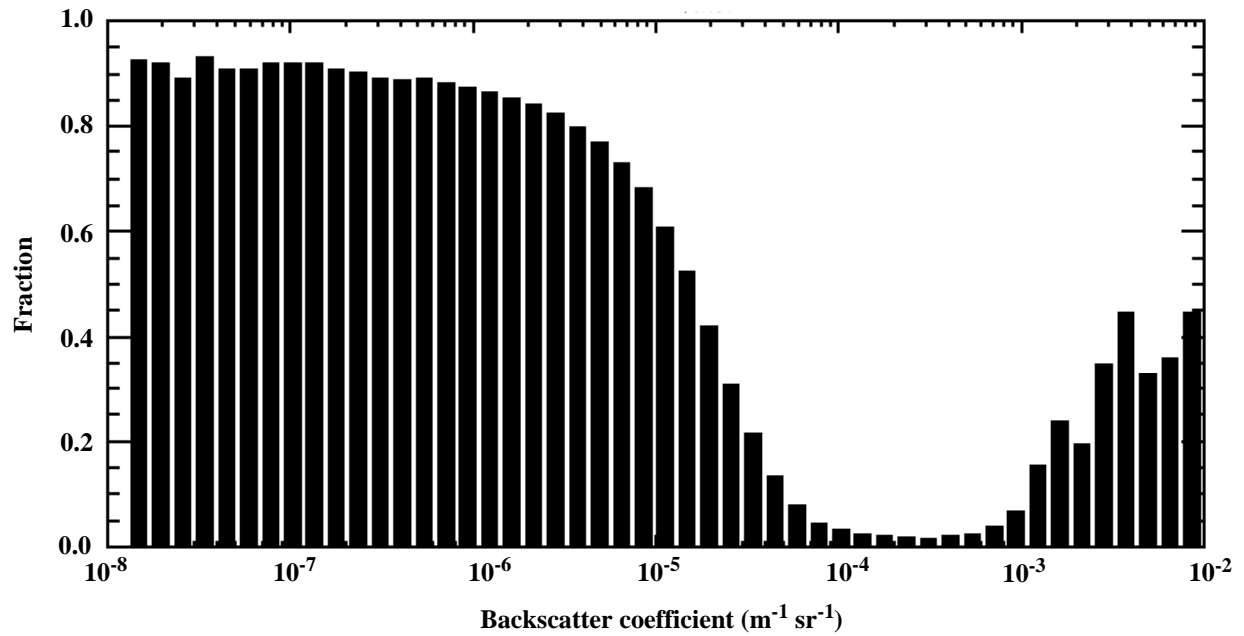


Figure 8: Distribution of backscatter coefficients from lidar in regions where the radar did not detect valid signal, for July 23, 2002. This is a distribution of backscatter missed by the radar, plotted as fraction of occurrences. The distribution turns upwards at high backscatter because the lidar detects low-level cumulus that the radar does not detect.

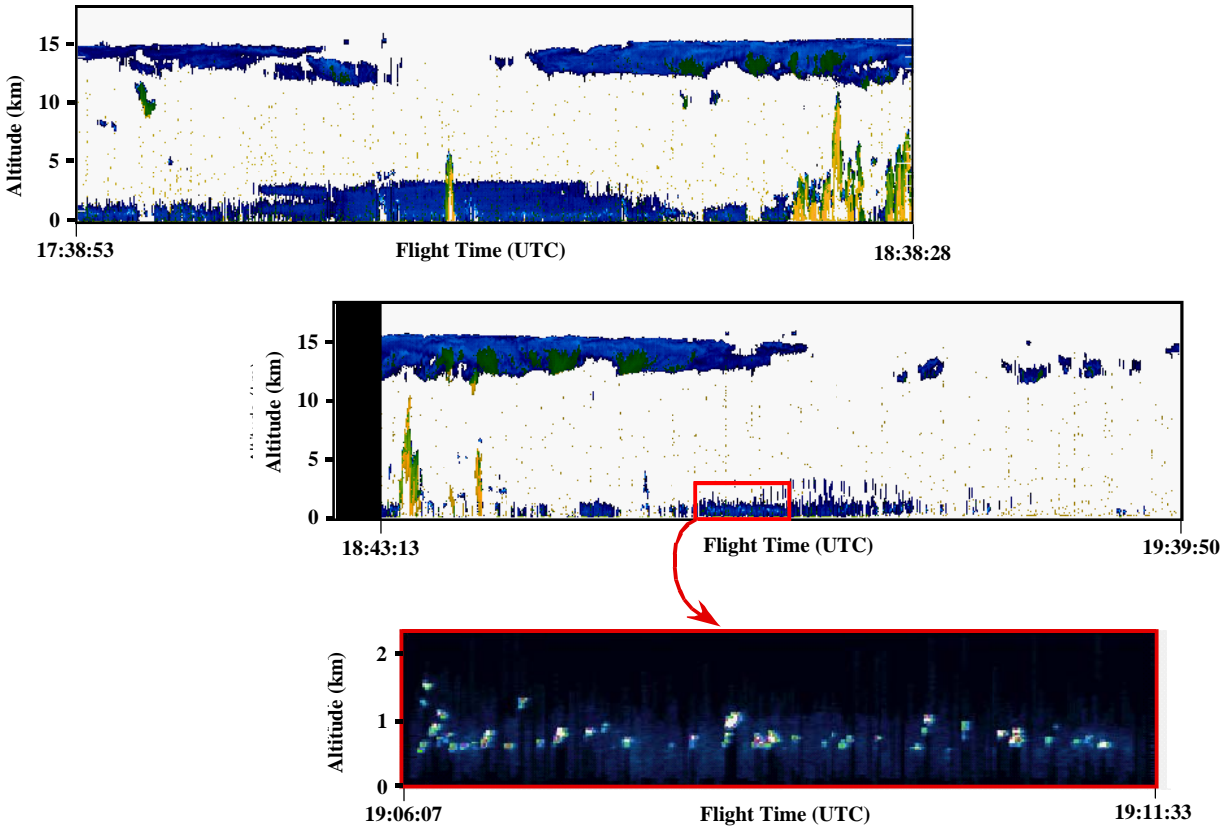


Figure 9: Composite image for July 26, 2002. Only the middle half of the flight is shown, as there was no radar signature in the early and later portions of the flight. The black region masks a 180-degree turn at the southern end of the flight track. Regions shaded in blue indicate lidar detection only, yellow indicates radar detection only, and green indicates both. Note that in contrast to the July 23 case, there is less measurement overlap in this example. The bottom panel is an enlarged view of the lowest 2 km over a short 5 minute segment showing that the lidar detected low-level cumulus of small vertical and spatial extent. Clouds are the white areas superposed on the marine boundary layer (in blue). Such cumulus are not detected by the radar owing to small particle size.

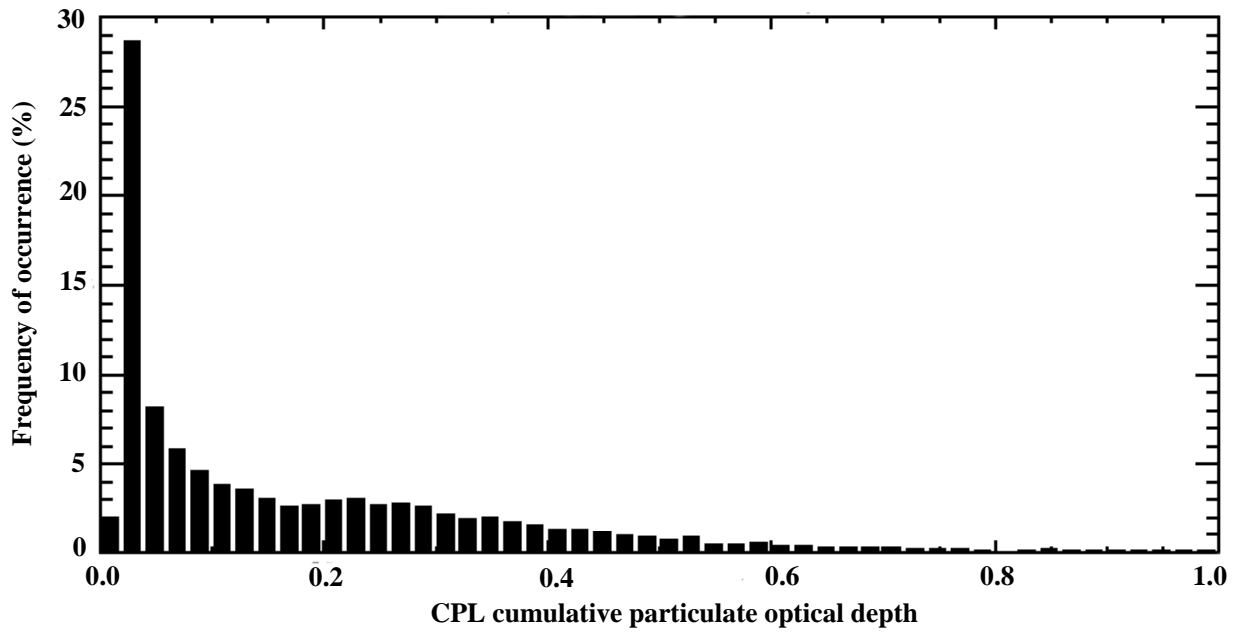


Figure 10: Occurrences of cumulative particulate optical depth derived from lidar measurements, for July 26, 2002. Histogram shows all optical depths missed by the radar (e.g. optical depth down to the first bin detected by radar, or entire profile if radar detected no signal). Compare with Figure 5 from July 23.

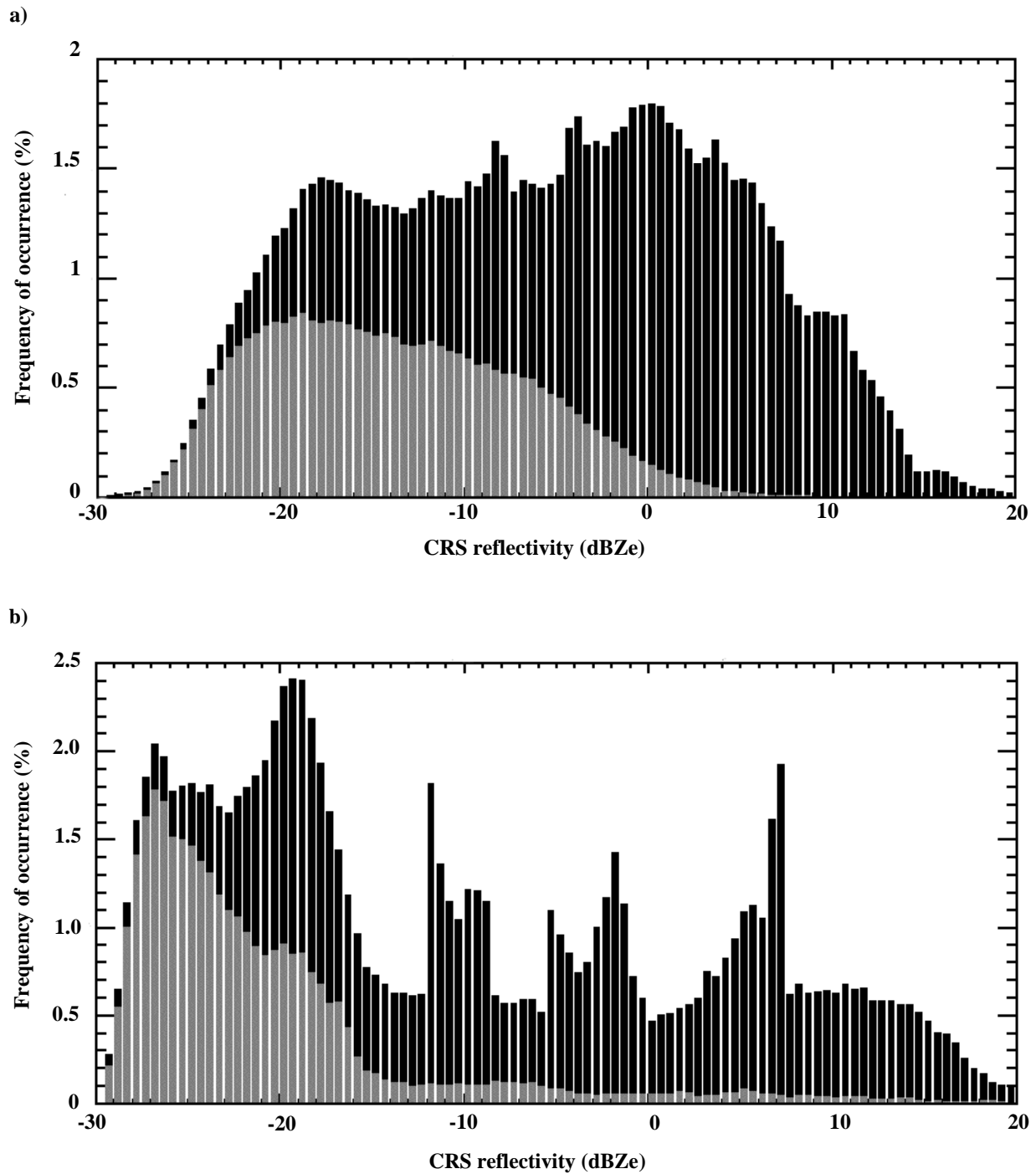


Figure 11: (a) Distribution of CRS radar reflectivity for July 23, 2002. (b) Same, for July 26, 2002. In each case, the black histogram is all bins detected by the radar. Overplotted in gray is the subset of bins from regions where the lidar also detected valid data.

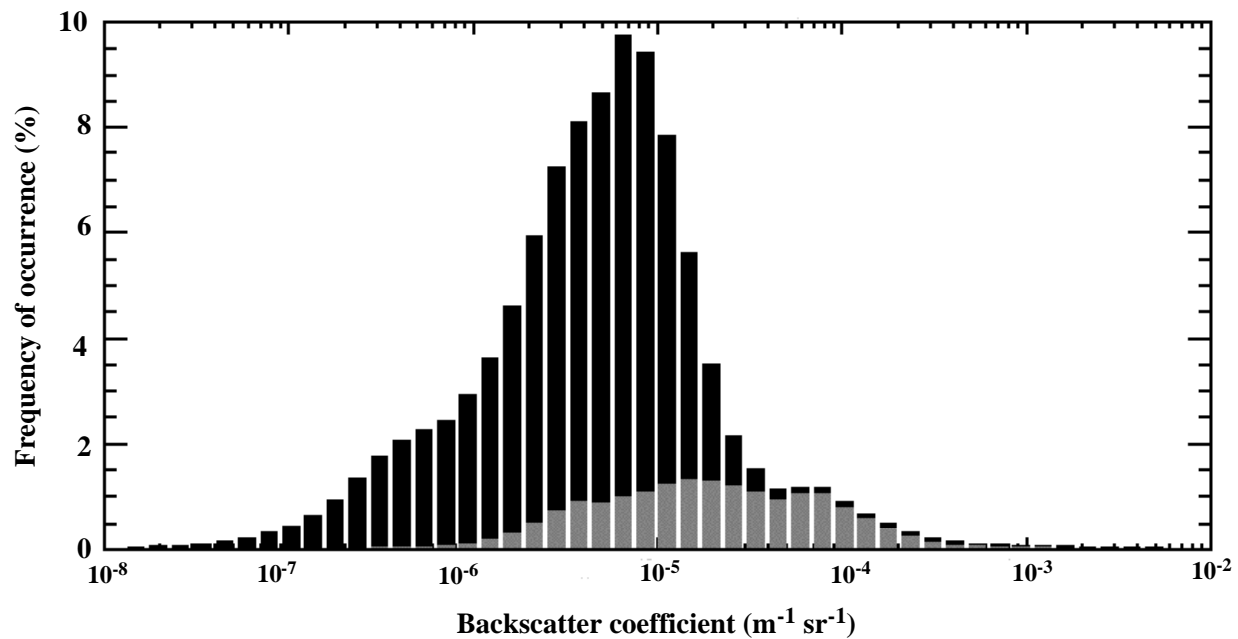


Figure 12: Distribution of backscatter coefficients from all lidar measurements within layers (black histogram), from July 26, 2002. Overplotted in gray is the subset detected by the lidar in regions where there was also valid radar signature (i.e., the instrument overlap). Compare with Figure 7 from July 23.

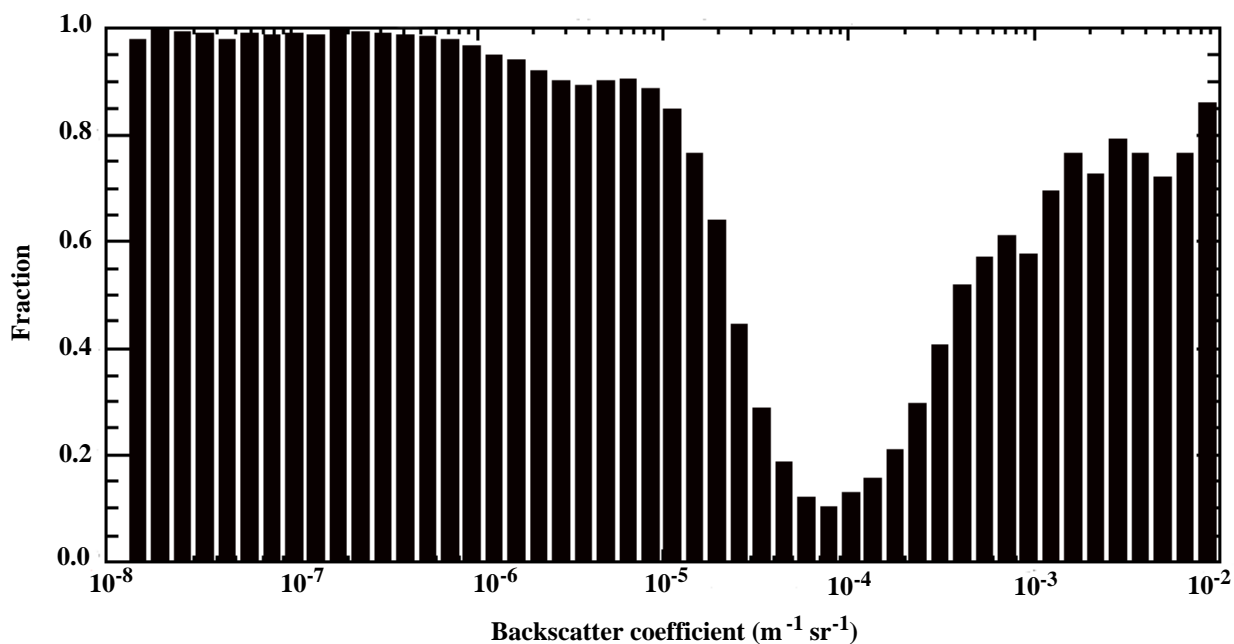


Figure 13: Distribution of backscatter coefficients from lidar in regions where the radar did not detect valid signal, for July 26, 2002. This is a distribution of backscatter missed by the radar, plotted as fraction of occurrences. The distribution turns upwards at high backscatter because on this day the lidar detected considerable low-level cumulus cloud that the radar does not detect, as illustrated in Figure 9. Compare with Figure 8 from July 23.